

## Supplementary Information

# Hydrocyclone-enhanced scalable photocatalytic hydrogen generation, from macroscale turbulence to nanoscale reaction dynamics

Danhui Yang<sup>1</sup>, Yizhou Yang<sup>1</sup>, Fanghe Zhou<sup>1</sup>, Zhuofan Deng<sup>1</sup>, Chuanjie Cui<sup>2</sup>, Jianping Li<sup>3, \*</sup>,  
Pengbo Fu<sup>1</sup>, Mingze Ma<sup>4</sup>, Wenjie Lv<sup>1</sup>, Zhengdai Zhang<sup>1</sup>, Xuejing Yang<sup>1, \*</sup>, Hualin Wang<sup>1, \*</sup>

1. National Engineering Research Center of Industrial Wastewater Detoxication and Resource Recovery, East China University of Science and Technology, Shanghai 200237, China
2. Department of Engineering Science, University of Oxford, Oxford OX1 3PJ, UK
3. College of Carbon Neutrality Future Technology, Sichuan University, Chengdu, 610207, PR China
4. College of General Aviation and Flight, Nanjing University of Aeronautics and Astronautics, Liyang 213300, China

\* Corresponding author

E-mail address:

[wanghl@ecust.edu.cn](mailto:wanghl@ecust.edu.cn) (H.W.).

[xj.yang@ecust.edu.cn](mailto:xj.yang@ecust.edu.cn) (X.Y.).

[lijianping1016@scu.edu.cn](mailto:lijianping1016@scu.edu.cn) (J.L.)

## 1. Chemicals

The original chemicals in catalyst preparation included:  $\text{CF}_3\text{COOH}$  (trifluoroacetic acid), phloroglucinol, hydrochloric acid, cetylpyridinium bromide, polyvinylpyrrolidone, tetrahydrofuran, and  $\text{H}_2\text{PtCl}_6$  (hydrogen hexachloroplatinate(IV)). All chemicals were of analytical grade and used as received without further purification.

## 2. Theory and Formula

### AQY and STH calculation details

The detailed formula for calculating AQY is as follows:

$$\text{AQY}(\%) = \frac{N_e}{N_p} \times 100\% = \frac{10^9(\nu N_A K)(hc)}{IS\lambda} \times 100\% \quad (1)$$

where  $\nu$  is the  $\text{H}_2$  evolution rate ( $3.34 \times 10^{-6} \text{ mol}\cdot\text{s}^{-1}$ );  $N_A$  is the Avogadro constant ( $6.02 \times 10^{23} \text{ mol}^{-1}$ );  $K$  is the number of electrons required per  $\text{H}_2$  molecule ( $K = 2$  for  $\text{H}_2$  evolution);  $h$  is the Planck constant ( $6.62 \times 10^{-34} \text{ J}\cdot\text{s}$ );  $c$  is the speed of light ( $3.0 \times 10^8 \text{ m}\cdot\text{s}^{-1}$ );  $I$  is the incident light intensity ( $300 \text{ W}\cdot\text{m}^{-2}$ ), measured by an optical power meter;  $S$  is the illuminated area ( $0.05 \text{ m}^2$ ); and  $\lambda$  is the irradiation wavelength (420 nm), after substituting the values, the result is 12.68%.

The detailed formula for calculating STH is as follows:

$$\text{STH} = \frac{r_{\text{H}_2} \times \varepsilon_{\text{H}_2}}{P_{\text{sun}} \times S} \quad (2)$$

where  $r_{\text{H}_2}$  is the hydrogen production rate ( $3.34 \times 10^{-6} \text{ mol}\cdot\text{s}^{-1}$ ),  $\varepsilon_{\text{H}_2}$  is the energy content of hydrogen ( $237 \text{ kJ mol}^{-1}$ ),  $P_{\text{sun}}$  is the solar energy flux ( $300 \text{ W}\cdot\text{m}^{-2}$ ), and  $S$  is the irradiated area ( $0.05 \text{ m}^2$ ), after substituting the values, the result is 5.28%.

### Multiscale theoretical model

The control equations of fluid field are modeled using the CFD  $k - \varepsilon$  turbulence framework, and particle dynamics, described within the DEM framework. Specifically, the transport equations for turbulent kinetic energy ( $k$ ) and its dissipation rate ( $\varepsilon$ ) are expressed as follows:

$$\frac{\partial(\rho k)}{\partial t} + \frac{\partial(\rho k u_i)}{\partial x_i} = \frac{\partial}{\partial x_j} \left[ \frac{\mu_t}{\sigma_k} \frac{\partial k}{\partial x_j} \right] + 2\mu_t E_{ij} E_{ij} - \rho \varepsilon \quad (3)$$

$$\frac{\partial(\rho \varepsilon)}{\partial t} + \frac{\partial(\rho \varepsilon u_i)}{\partial x_i} = \frac{\partial}{\partial x_j} \left[ \frac{\mu_t}{\sigma_\varepsilon} \frac{\partial \varepsilon}{\partial x_j} \right] + C_{1\varepsilon} \frac{\varepsilon}{k} 2\mu_t E_{ij} E_{ij} - C_{2\varepsilon} \rho \frac{\varepsilon^2}{k} \quad (4)$$

where  $\rho$  is the fluid density,  $u_i$  the velocity component,  $\mu_t$  the turbulent viscosity, and  $E_{ij}$  the strain-rate tensor. The coefficients  $\sigma_k$ ,  $\sigma_\varepsilon$ ,  $C_{1\varepsilon}$ , and  $C_{2\varepsilon}$  are the standard empirical constants in the  $k - \varepsilon$  model.

For the DEM describing the particle dynamics, both rotational and translational motions are considered. The rotational equation of motion of the  $i$ -th particle is:

$$I_i \frac{d\omega_i}{dt} = \sum_{j=1}^k (T_{t,ij} + T_{r,ij}) \quad (5)$$

where  $I_i$  denotes the moment of inertia,  $\omega_i$  is the angular velocity,  $T_{t,ij}$  and  $T_{r,ij}$  are the tangential and rolling torques due to contact with the  $j$ -th neighbor, and  $k$  is the total number of particles, respectively. The translational motion is governed by the net force balance:

$$F_i^M = f_{pf,i} + \sum_{i=1}^{k-1} f_{pp,i} + m_i g \quad (6)$$

where  $F_i^M$  is the total force on particle  $i$ ,  $f_{pf,i}$  is the fluid-particle interaction force,  $f_{pp,i}$  is the contact force from neighboring particles,  $m_i$  is the mass of the particle, and  $g$  is the gravitational acceleration.

### Note on averaged force

To represent the macro-scale loading imposed by a given flow velocity, we use the time-averaged force for component  $i$ :

$$\bar{F}_i = \frac{1}{N_t} \sum_{k=1}^{N_t} F_i(t_k) \quad (7)$$

where  $F_i(t_k)$  is the instantaneous force sampled at times  $t_k$  over a statistically steady window of length  $N_t$ . This time average filters out high-frequency fluctuations that are not resolved at the macro scale and yields an effective driving load associated with the operating condition. In contrast, instantaneous or maximum forces can be strongly intermittent and may overstate the typical load for a fixed velocity. We therefore report  $\bar{F}_i$  as the primary descriptor, together with its sampling uncertainty.

### Particle-packing model (Dense Sphere Packing, DSP)

We generated random, non-overlapping sphere packings in a cubic RVE ( $V_{\text{RVE}} = L^3$ ) using Digimat's DSP algorithm. For a prescribed radius set  $\{r_i\}_{i=1}^N$  and target packing fraction  $\phi_{\text{target}}$ , the configuration satisfies:

#### Packing fraction

$$\phi = \frac{1}{V_{\text{RVE}}} \sum_{i=1}^N \frac{4}{3} \pi r_i^3 \approx \phi_{\text{target}} \quad (8)$$

#### Non-overlap

$$\| \mathbf{x}_i - \mathbf{x}_j \|_{\min} \geq r_i + r_j \quad (\forall i \neq j) \quad (9)$$

The algorithm iteratively relaxes sphere positions until the non-overlap constraint is met and  $|\phi - \phi_{\text{target}}| \leq \varepsilon_\phi$ . Compared with Random Sequential Addition (RSA), DSP more reliably reaches higher  $\phi$  while maintaining randomness, making it suitable for representative RVEs.

### AIMD stability test

We assessed equilibration by monitoring the AIMD potential-energy trace at each strain and required a stationary fluctuation window before applying the next +2% biaxial increment. The simulation process is divided into 4 phases:

5% strain (Fig. S16(a)): After an initial pre-equilibration, the potential energy fluctuates within  $\pm 0.1$  Hartree over the final 1 ps (1000 steps at 1 fs), indicating a steady state.

Transition at 7% (Fig. S16(b)): An energetic step is observed between 1450–1650 fs, corresponding to a Pt–ligand (Pt–N  $\rightarrow$  Pt–C) coordination change. The event completes within  $\sim 200$  fs, after which the energy returns to stationary fluctuations within the subsequent 300 fs window.

7–9% strain (Fig. S16(c)): No further structural transitions are detected; the energy remains within  $\pm 0.1$  Hartree, satisfying our stability criterion.

11% strain (Fig. S16(d)): A sharp energy drop at  $\sim 3500$  fs marks fracture of the COF ring network, as discussed in the manuscript.

Together, these traces show that 1 ps of pre-equilibration at each strain increment is sufficient to reach a stationary regime, and that any strain-induced rearrangements occur on sub-picosecond timescales and are captured before the next increment.

### Incremental dynamical stability criteria

we establish incremental dynamical stability at 7% strain by two standard criteria, accompanied by detailed computational procedures:

#### (1) Positive-definite tangent 2D stiffness (Born criteria)

Statement of the criterion: At a prescribed pre-strain  $\varepsilon_0$  (cell fixed in-plane; internal coordinates relaxed), the incremental/tangent 2D stiffness  $C^{2D}$  (plane stress) must be positive definite. For an orthotropic 2D membrane in Cartesian axes  $(x, y)$ ,

$$C^{2D} = \begin{pmatrix} C_{11} & C_{12} \\ C_{12} & C_{22} \end{pmatrix}, \quad C_{66} > 0 \quad (10)$$

and the Born stability conditions are:

$$C_{11} > 0, \quad C_{22} > 0, \quad C_{66} > 0, \quad C_{11}C_{22} - C_{12}^2 > 0.$$

We compute  $C_{ij}^{2D}$  from VASP stresses:

Using central finite differences about  $\varepsilon_0$  with small Cartesian perturbations (uniaxial  $\pm \Delta$  in  $x$  or  $y$ ; and engineering shear  $\gamma = \pm \Delta_\gamma$ , we obtain:

$$\begin{aligned}
C_{11}^{2D} &\approx -\frac{\sigma_{xx}^{3D}(+\Delta\varepsilon_{xx}) - \sigma_{xx}^{3D}(-\Delta\varepsilon_{xx})}{2\Delta} L_z 10^{-2}, \\
C_{22}^{2D} &\approx -\frac{\sigma_{yy}^{3D}(+\Delta\varepsilon_{yy}) - \sigma_{yy}^{3D}(-\Delta\varepsilon_{yy})}{2\Delta} L_z 10^{-2}, \\
C_{12}^{2D} &\approx -\frac{\sigma_{yy}^{3D}(+\Delta\varepsilon_{xx}) - \sigma_{yy}^{3D}(-\Delta\varepsilon_{xx})}{2\Delta} L_z 10^{-2}, \\
C_{66}^{2D} &\approx -\frac{\sigma_{xy}^{3D}(+\gamma) - \sigma_{xy}^{3D}(-\gamma)}{2\gamma} L_z 10^{-2}.
\end{aligned} \tag{11}$$

Here  $\sigma_{ij}^{3D}$  are the VASP stresses from the in kB block (Table. Rx),  $L_z$  is the vacuum-included cell height in Å (here  $L_z = 25$  Å),  $\Delta = 0.002$  ( $\pm 0.2\%$  uniaxial),  $\Delta\gamma = 0.002$  ( $\pm 0.2\%$  engineering shear) and the factor  $10^{-2}$  converts  $\text{kB} \times \text{Å}$  to N/m since  $1 \text{ kB} = 108 \text{ Pa}$ .

**Table. S1** Raw stresses from OUTCAR (kB)

Case	$\sigma_{xx}$	$\sigma_{yy}$	$\sigma_{xy}$
Baseline	-8.55903	-8.57052	-1.79438
x + 0.2%	-8.70080	-8.55234	-1.79010
x - 0.2%	-8.38975	-8.54638	-1.79966
y + 0.2%	-8.54441	-8.70824	-1.79026
y - 0.2%	-8.53642	-8.39349	-1.79968
shear + 0.2% $\gamma$	-8.53774	-8.54705	-1.79601
shear - 0.2% $\gamma$	-8.53760	-8.54624	-1.79568

Tangent 2D stiffness results (N/m):  $C_{11} = 19.44$ ,  $C_{22} = 19.67$ ,  $C_{12} = 0.44$ ,  $C_{66} = 8.68$ , so  $C_{11} > 0$ ,  $C_{22} > 0$ ,  $C_{66} > 0$  and  $C_{11}C_{22} - C_{12}^2 > 0$ , hence  $C^{2D}$  is positive-definite at 7% pre-strain.

## (2) Positive acoustic tensor under the measured pre-stress

Statement of the criterion: At a prescribed pre-strain  $\varepsilon_0$  with in-plane pre-stress  $\tau^{2D}$ , incremental dynamical stability requires the acoustic tensor

$$\Gamma_{ik}(\mathbf{n}) = \frac{1}{\rho_{2D}} (C_{ijkl}^{2D} n_j n_l + \tau_{jl}^{2D} \delta_{ik} n_j n_l) \tag{12}$$

to be positive definite for every in-plane direction  $\mathbf{n} = (\cos\theta, \sin\theta)$ ; equivalently, both eigenvalues  $v_m^2(\theta)$  are positive (real wave speeds) for all  $\theta \in [0, 2\pi)$ .

Directional form for an orthotropic 2D membrane. (With Voigt notation)

$$\mathbf{C}^{2D} = \begin{pmatrix} C_{11} & C_{12} & 0 \\ C_{12} & C_{22} & 0 \\ 0 & 0 & C_{66} \end{pmatrix}, \quad \boldsymbol{\tau}^{2D} = \begin{pmatrix} \tau_{xx} & \tau_{xy} \\ \tau_{xy} & \tau_{yy} \end{pmatrix} \quad (13)$$

define  $s(\theta) = \mathbf{n}^T \boldsymbol{\tau}^{2D} \mathbf{n}$ . The projected stiffness entering  $\Gamma$  is

$$\mathbf{n} : \mathbf{C}^{2D} : \mathbf{n} = \begin{pmatrix} C_{11}\cos^2\theta + C_{66}\sin^2\theta & (C_{12} + C_{66})\sin\theta\cos\theta \\ (C_{12} + C_{66})\sin\theta\cos\theta & C_{22}\sin^2\theta + C_{66}\cos^2\theta \end{pmatrix} \quad (14)$$

so that  $\rho_{2D}\Gamma(\mathbf{n}) = (\mathbf{n} : \mathbf{C}^{2D} : \mathbf{n}) + s(\theta)\mathbf{I}_2$ . The requirement “ $\Gamma(\mathbf{n}) > 0$  for all  $\theta$ ” is exactly the wave-propagation (WP) / strong-ellipticity condition used today to certify incremental stability under finite pre-stress.

Verification (direction-independent lower bound)

The smallest eigenvalue of the in-plane block is

$$\lambda_{\min}(\mathbf{C}^{2D}) = \frac{C_{11} + C_{22} - \sqrt{(C_{11} - C_{22})^2 + 4C_{12}^2}}{2} \approx 19.1 \text{ N/m} > 0.$$

For any  $\theta$ , with  $s(\theta) \in [-2.15, -2.13] \text{ N/m}$ ,

$$\lambda_{\min}(\rho_{2D}\Gamma(\mathbf{n})) \geq \lambda_{\min}(\mathbf{C}^{2D}) + s(\theta) \gtrsim 19.1 - 2.15 = 16.9 \text{ N/m} > 0.$$

Therefore,  $\Gamma(\mathbf{n})$  is positive for all directions, implying real incremental wave speeds and establishing incremental dynamical stability at 7% pre-strain.

These mechanics-based results are consistent with our finite-temperature AIMD at strains  $\leq 7\%$ , which show no spontaneous reconstruction or bond scission over the simulation windows, while fracture occurs only near  $\sim 11\%$ . Together, they define a physically meaningful stability window of 0–7% strain for the COF considered here.

### 3. Figures

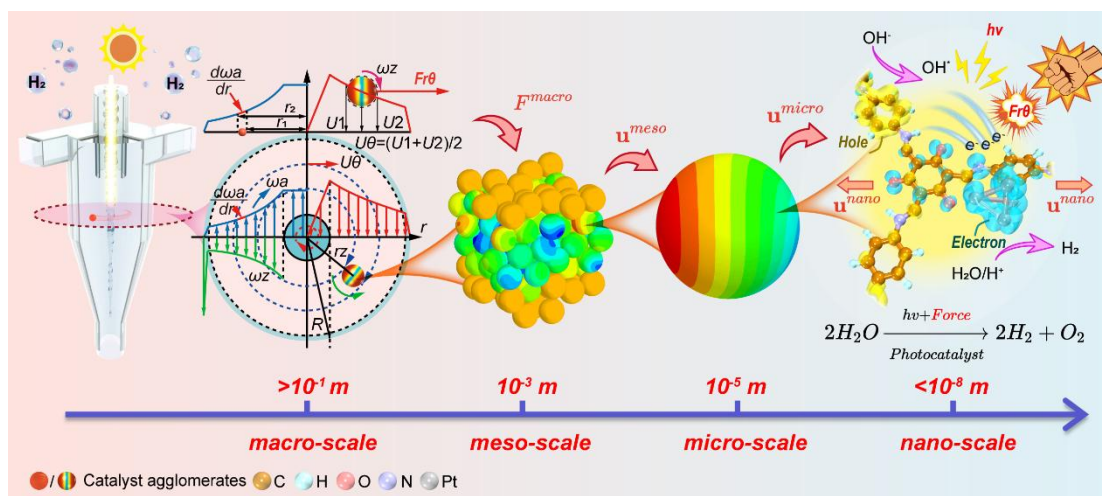


**Fig. S1** Multiscale framework for hydrocyclone-enhanced solar hydrogen generation.

**Extended caption:** The scheme illustrates the hierarchical transfer of hydrodynamic forces generated by the macroscale hydrocyclone flow to lattice-level distortions at the catalyst surface. At the macro scale ( $>10^{-1}$  m), catalyst particles are entrained by the intense turbulent swirling field, undergoing translation and rotation while experiencing strong hydrodynamic loading. A representative radial cross-section of the hydrocyclone is used to depict the velocity distributions and force environment: the blue curve shows the circumferential velocity distribution associated with particle orbital motion characterized by the angular velocity  $\omega a$ , the red curve shows the fluid circumferential velocity  $U\theta$ , and the green curve indicates the particle self-rotation angular velocity  $\omega z$ . A particle located at radial position  $r$  experiences a resultant hydrodynamic force  $F^{macro}$ , which is transmitted downscale and manifests as a mesoscale deformation/strain field  $u^{meso}$  within catalyst agglomerates, then as a microscale deformation field  $u^{micro}$  for an individual particle, and ultimately as a nanoscale lattice distortion  $u^{nano}$  at surface lattice atoms. These strain-induced lattice perturbations are further coupled to photoexcitation and interfacial charge separation on the photocatalyst, thereby impacting the reaction pathway of solar-driven water splitting. All modeling schematics and symbols shown here are based on the theoretical derivations and numerical calculations presented in the main text.





**Fig. S2** Photograph of Hydrocyclone-based Photocatalytic Reactor.

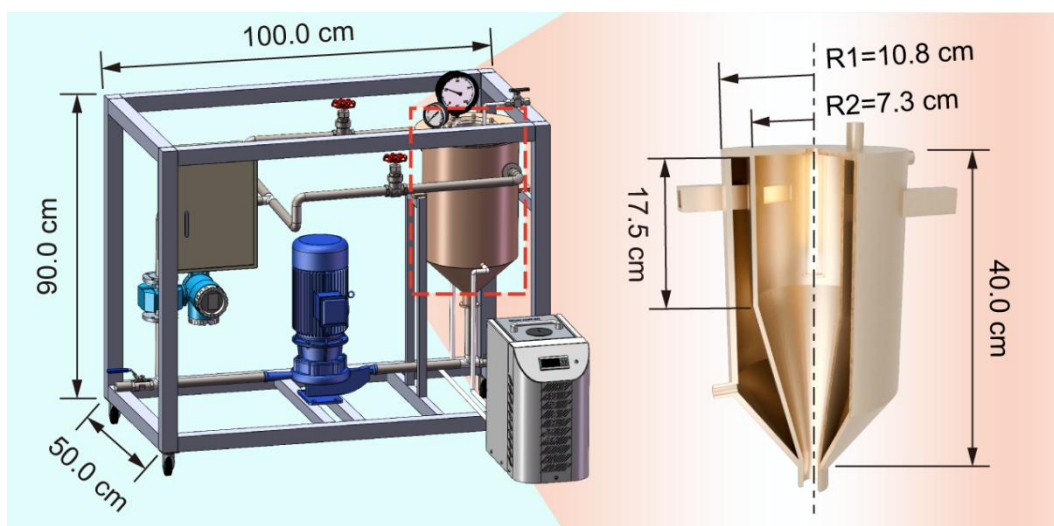


**Fig. S3** Dimensioned schematic of the hydrocyclone-based photocatalytic reactor.

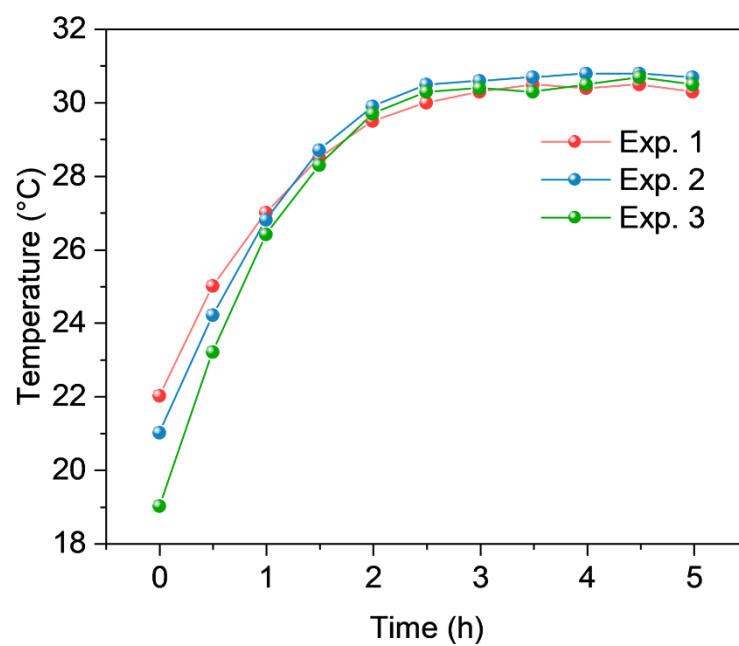


**Fig. S4** Temperature evolution of the reaction liquid.

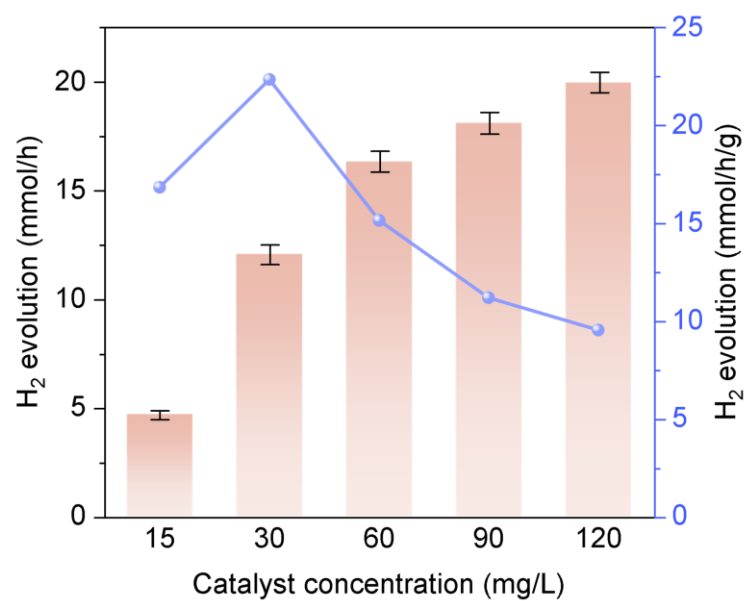


**Fig. S5** Comparison of hydrogen production with different catalyst concentrations at a flow rate of 40 L/min.

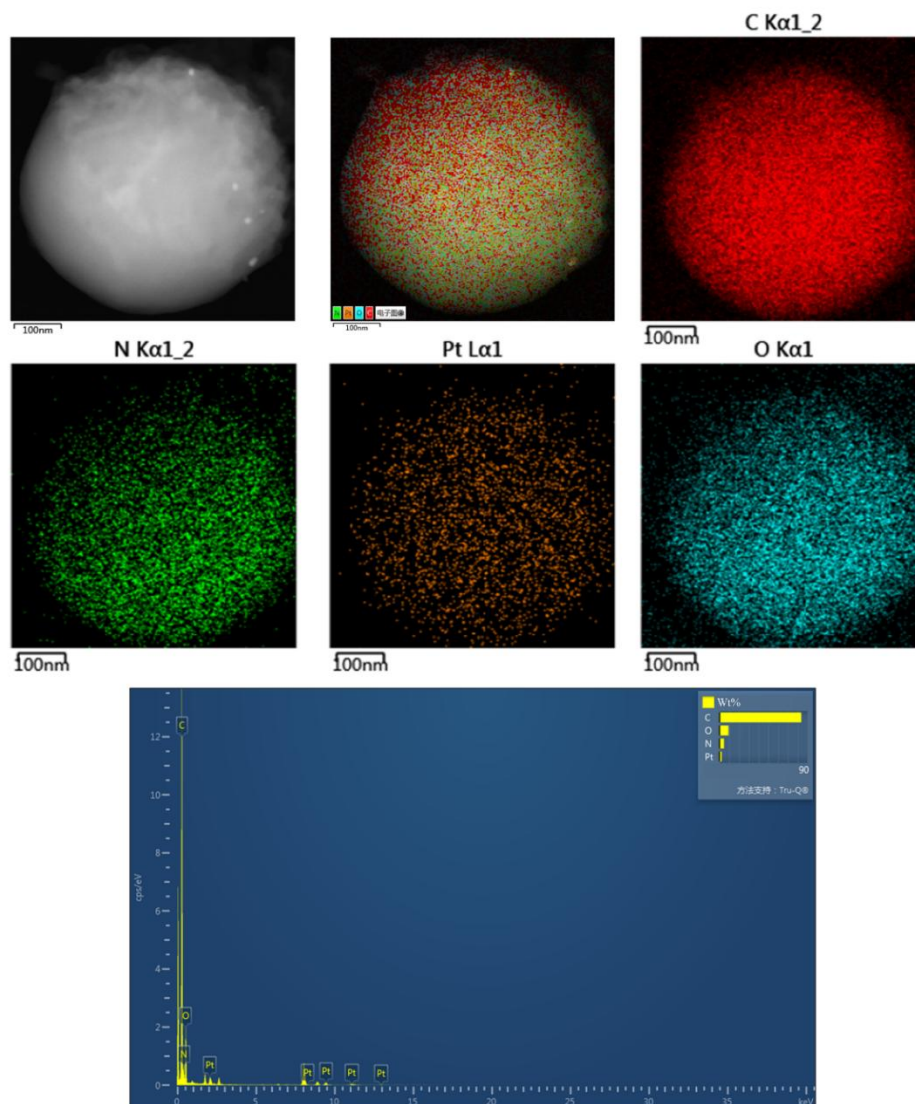


**Fig. S6** EDS analysis of Pt-COF: color-coded elemental mappings (red: C, green: N, orange: Pt, cyan: O) with Pt content of 1 wt%.

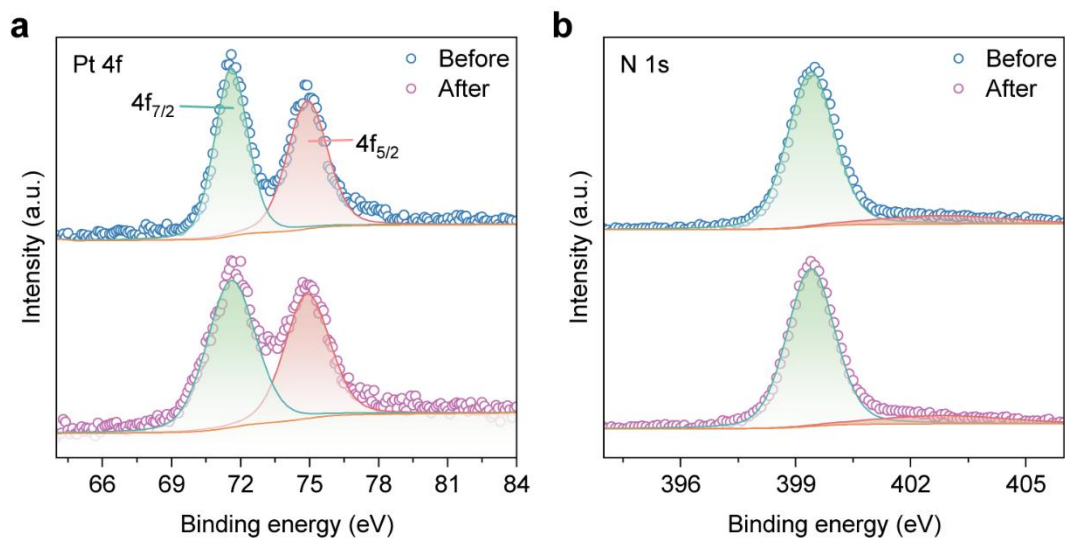


**Fig. S7** XPS spectra of Pt-COF before and after hydrocyclone operation: (a) Pt  $4f$  and (b) N  $1s$ .

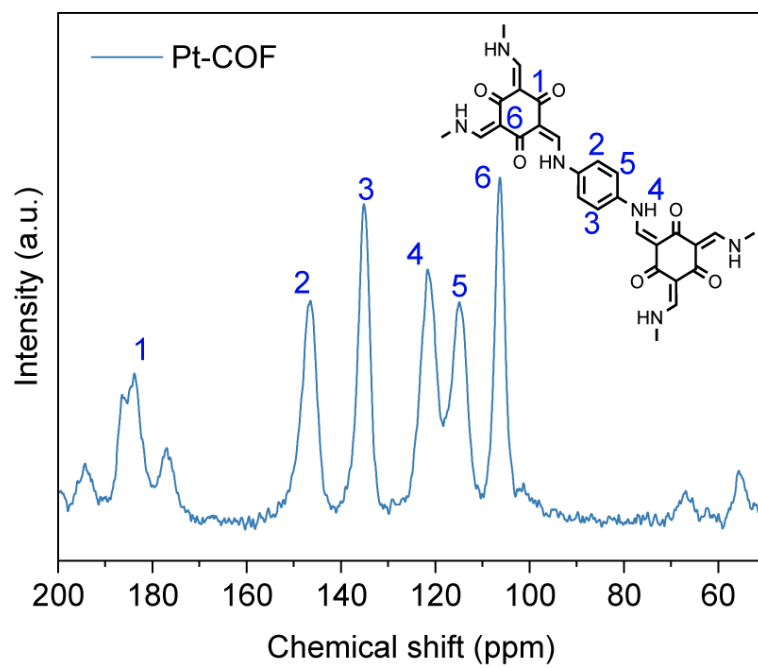


**Fig. S8** Solid-state CP-MAS  $^{13}\text{C}$  NMR spectra of Pt-COF.

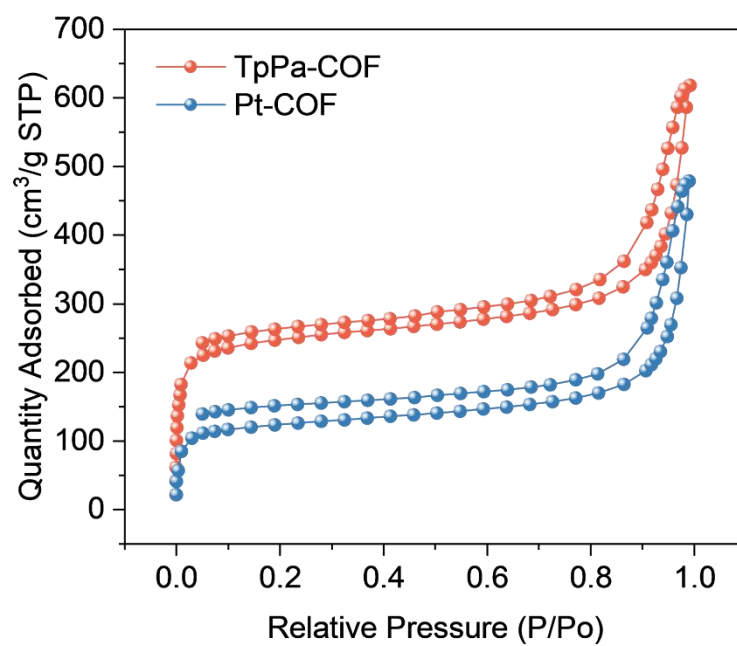


**Fig. S9** N<sub>2</sub> adsorption and desorption isotherms (77 K) of TpPa-COF and Pt-COF.



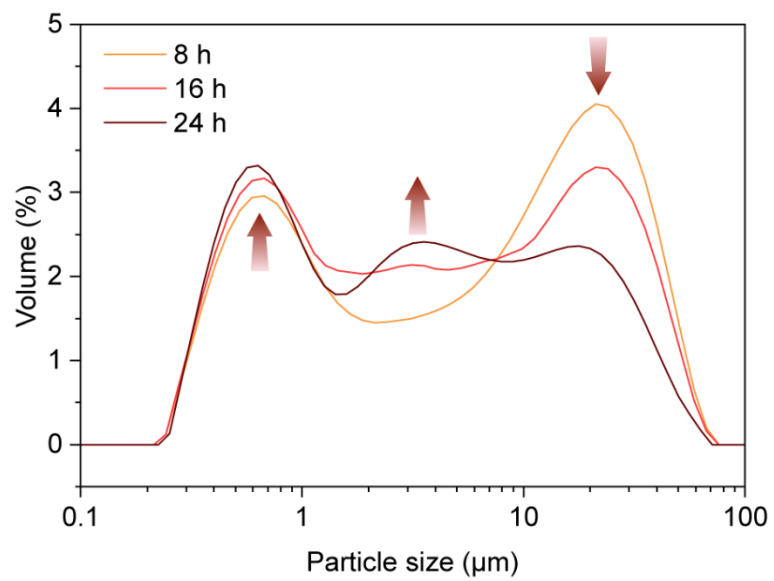


**Fig. S10** PSD of the reaction slurry at 6 h, 12 h, and 18 h measured by Malvern laser diffraction.

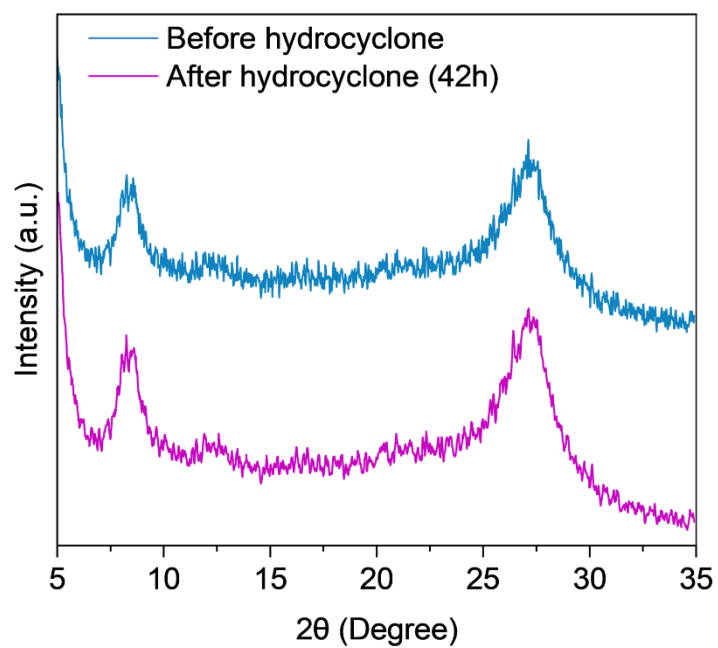


**Fig. S11** XRD of Pt-COF before and after hydrocyclone operation.

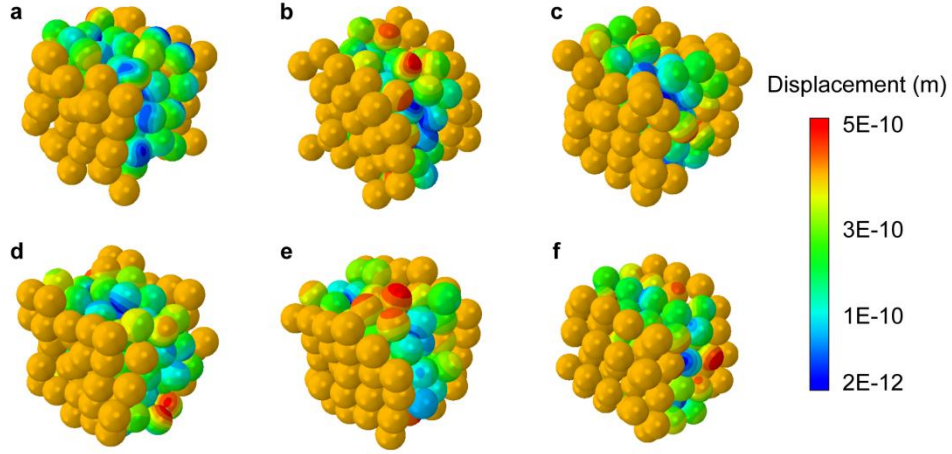


**Fig. S12** Sensitivity of displacement fields to sub-particle configurations. Panels (a-f) show six independent stochastic realizations with different sub-particle counts ( $N$ ): (a)  $N = 117$ , (b)  $N = 119$ , (c)  $N = 120$ , (d)  $N = 121$ , (e)  $N = 122$ , and (f)  $N = 128$ .

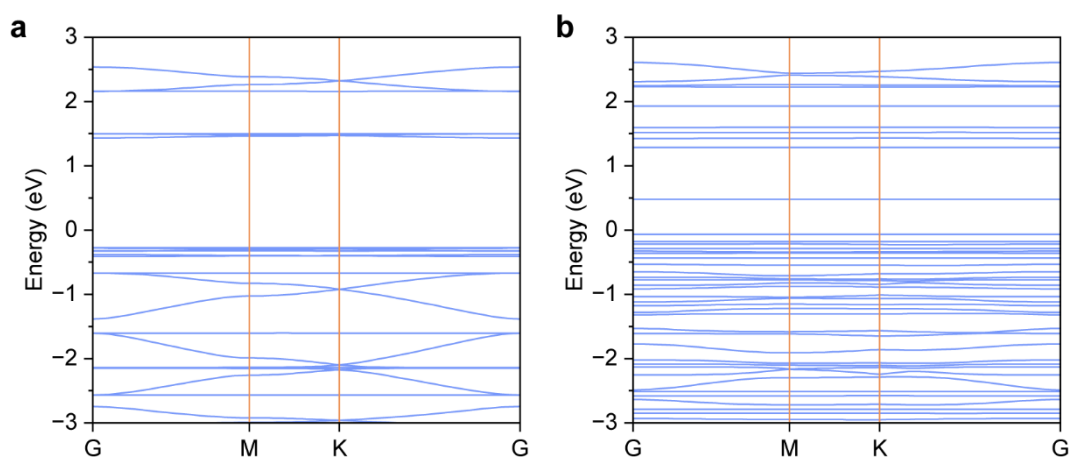


**Fig. S13** Band structures of (a) TpPa-COF and (b) Pt-COF.

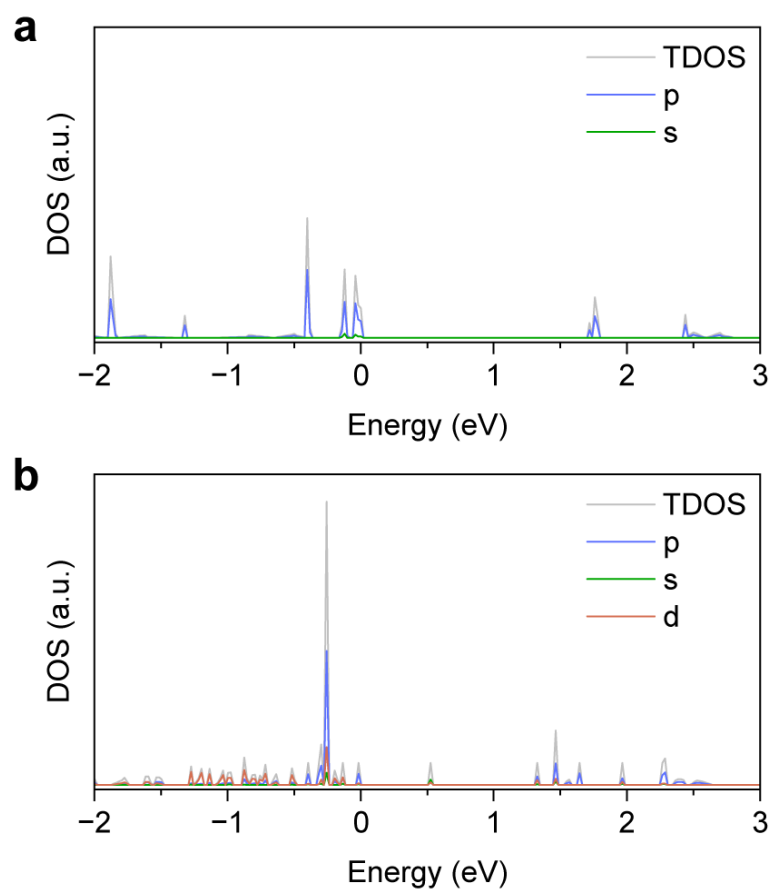


**Fig. S14** Total and projected DOS of (a) TpPa-COF and (b) Pt-COF.

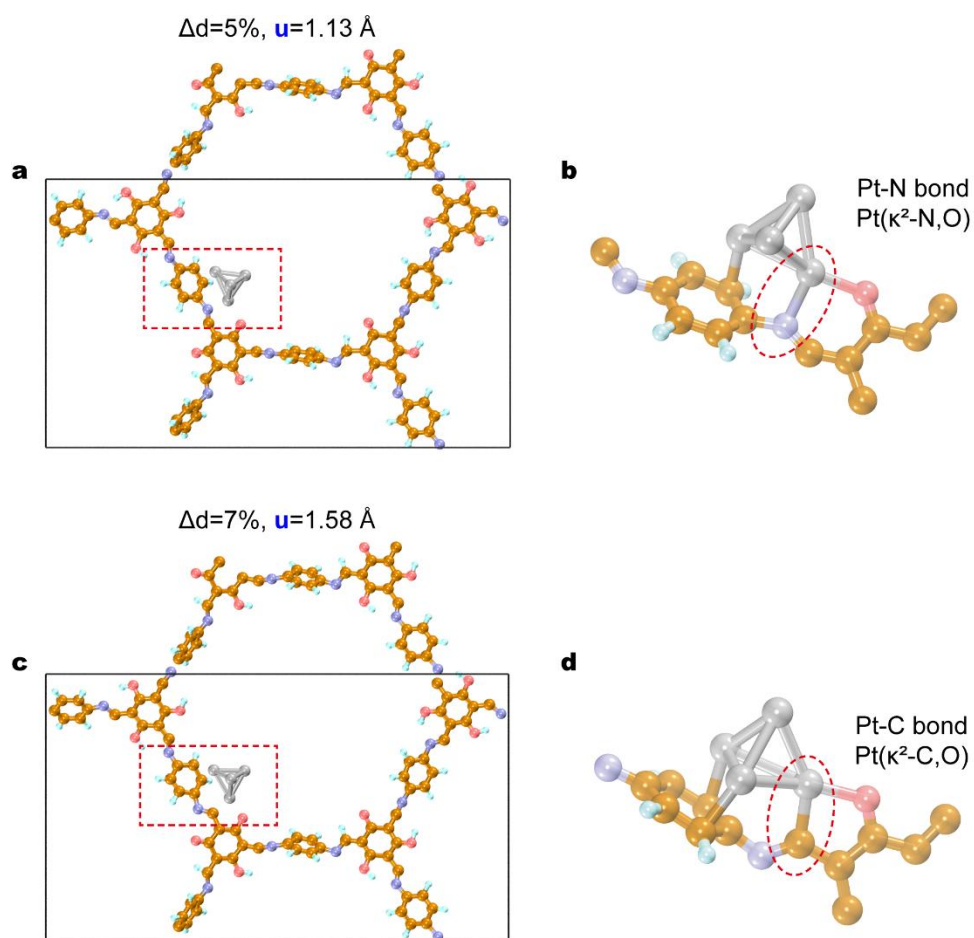


**Fig. S15** (a, b) Pt–N coordination under 5% strain transitioning to (c, d) Pt–C coordination at 7% strain.

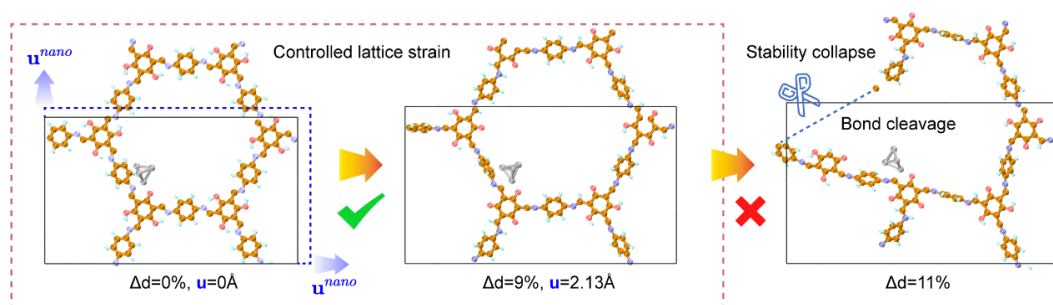


**Fig. S16** AIMD-simulated lattice stretching evolution: controlled strain phase and post-overstretching bond cleavage/stability collapse stages.

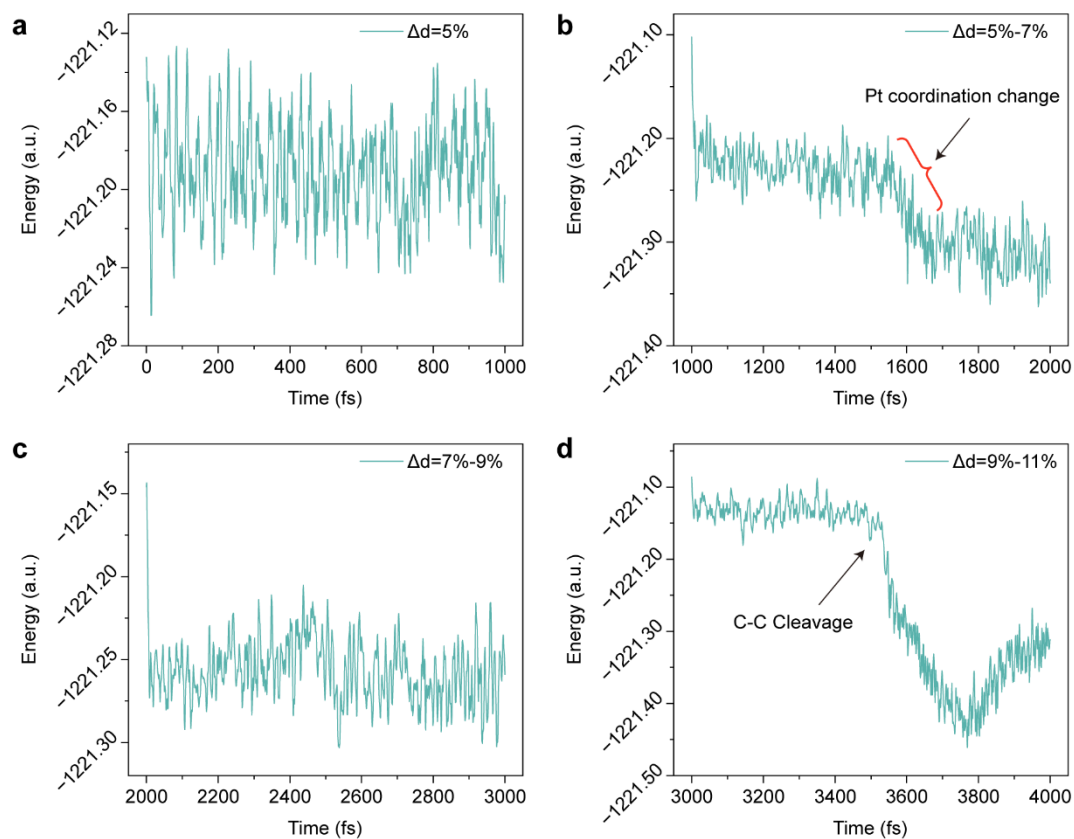


**Fig. S17** Potential energy fluctuations during AIMD under tensile strain: (a) 5%, (b) 7%, (c) 9%, (d) 11%.



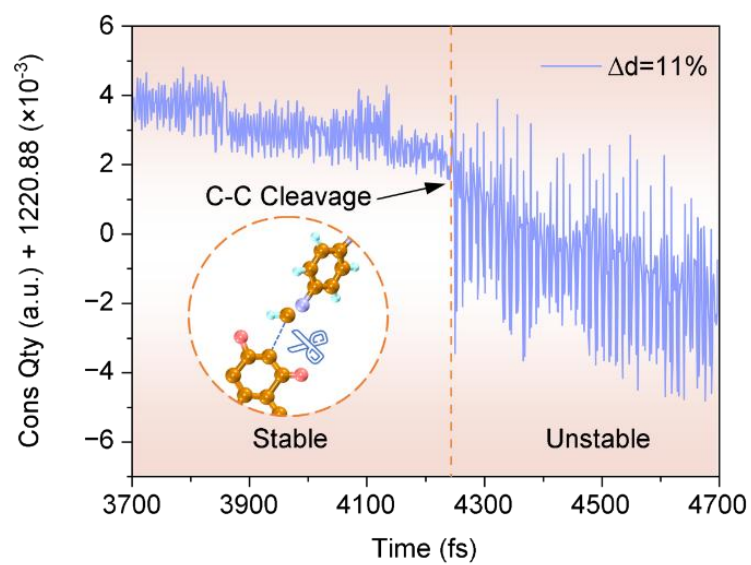


**Fig. S18** Conserved quantity evolution during AIMD-simulated C–C bond cleavage event.

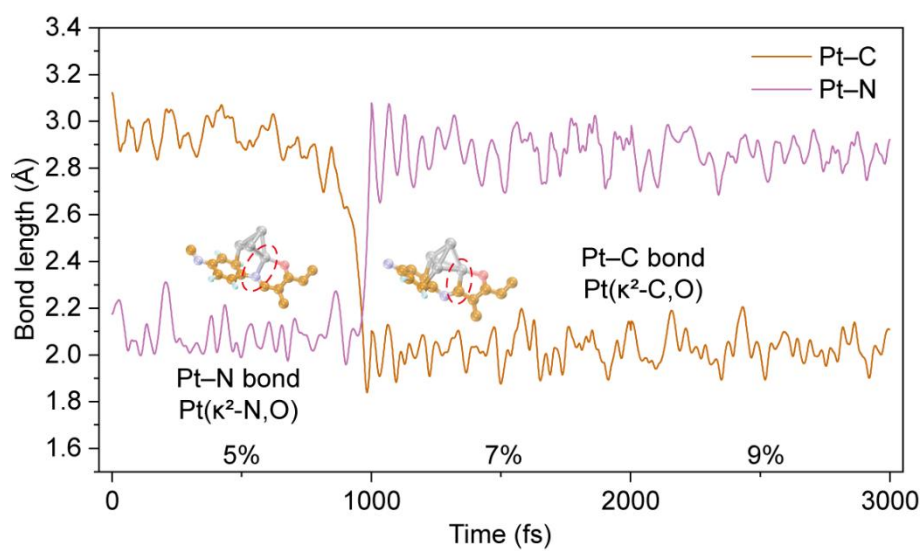


**Fig. S19** Time-resolved Pt-C and Pt-N bond-length variations during AIMD.

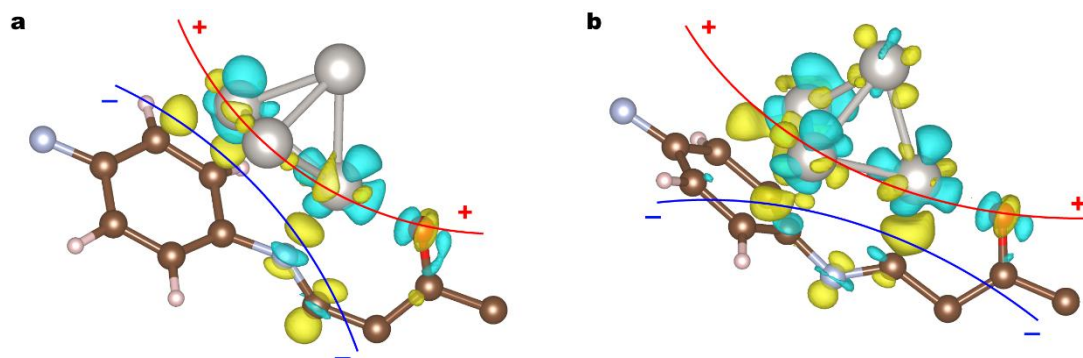


**Fig. S20** Differential charge density at (a) 5% and (b) 7% strains (isovalue = 0.01  $e/\text{\AA}^3$ ). The blue regions represent charge depletion, while the yellow areas indicate charge accumulation.

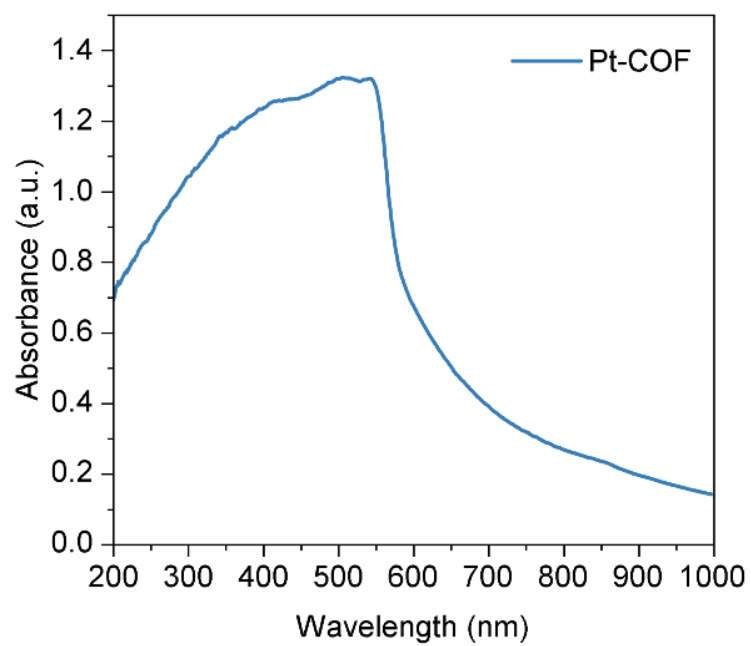


**Fig. S21** Optical absorption spectra of Pt-COF.

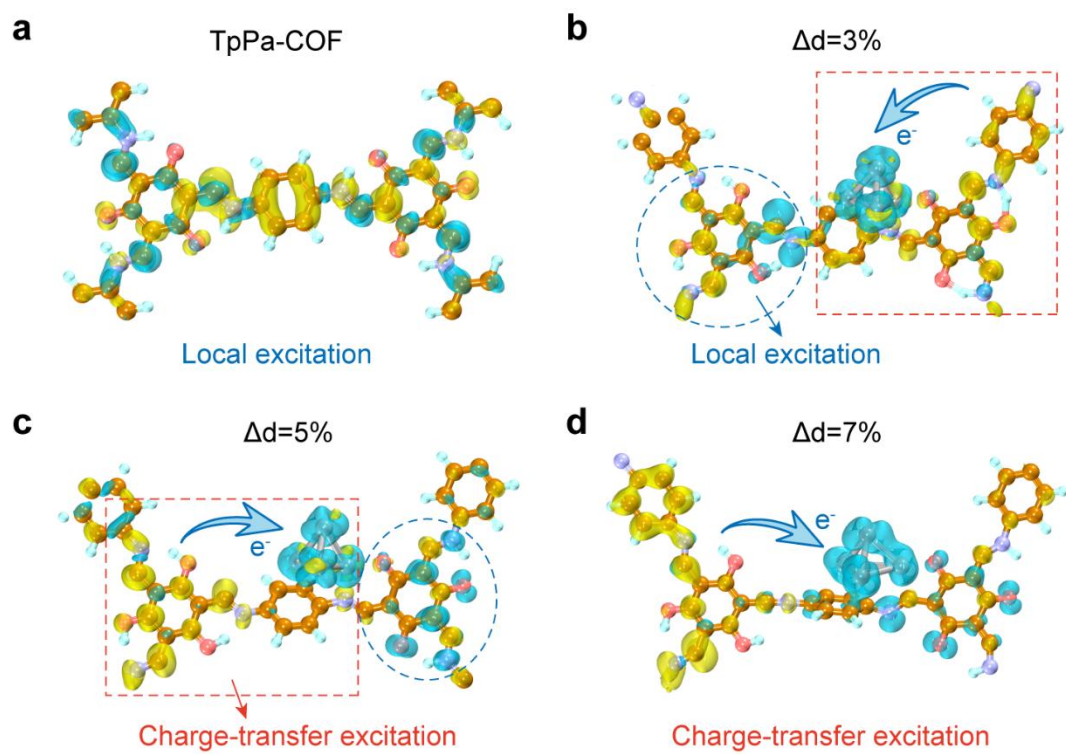


**Fig. S22** TDDFT electron-hole distributions at different lattice strains: (a) TpPa-COF, (b) 3%, (c) 5%, (d) 7%.

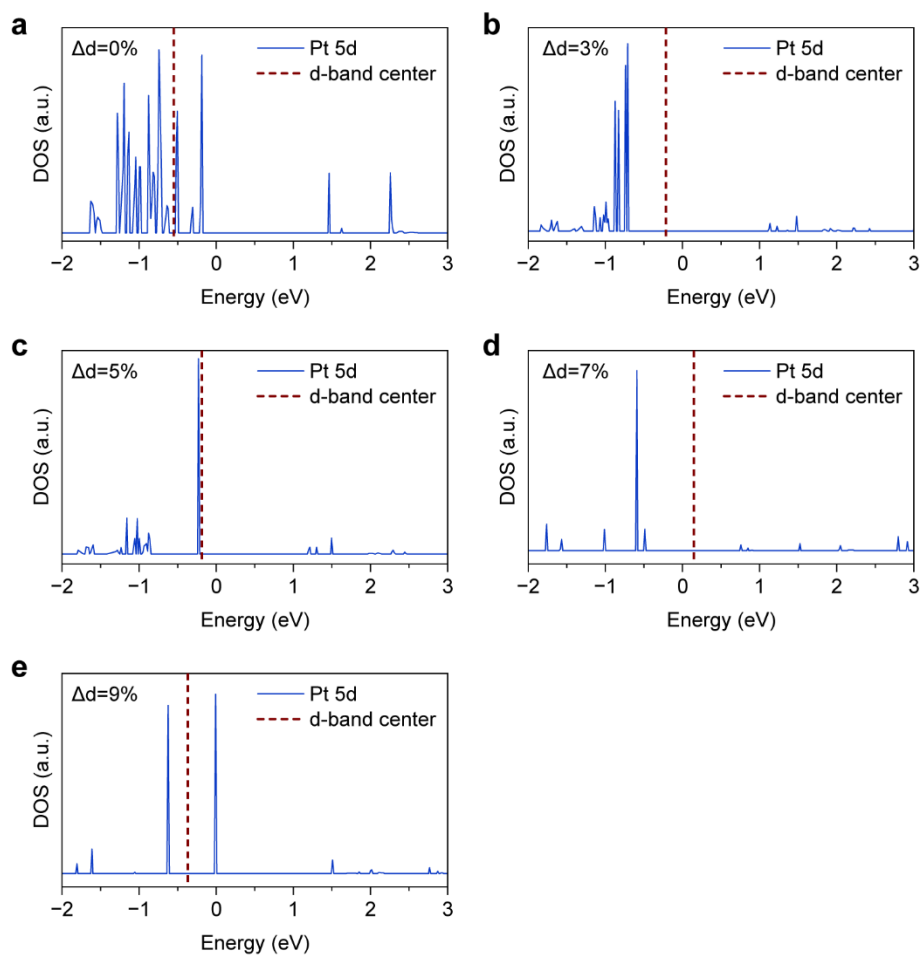


**Fig. S23** DOS of Pt-COF under different lattice strains: (a) 0%, (b) 3%, (c) 5%, (d) 7% and (e) 9%.

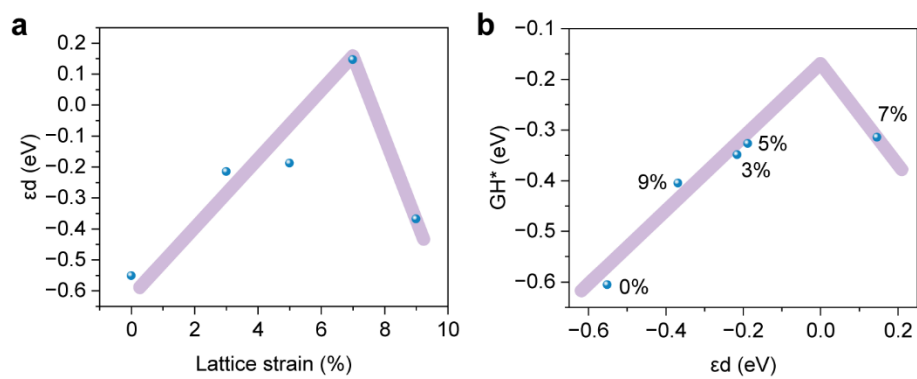


**Fig. S24** (a) d-band center versus lattice strain; (b) Relationship between d-band center and  $GH^*$ .

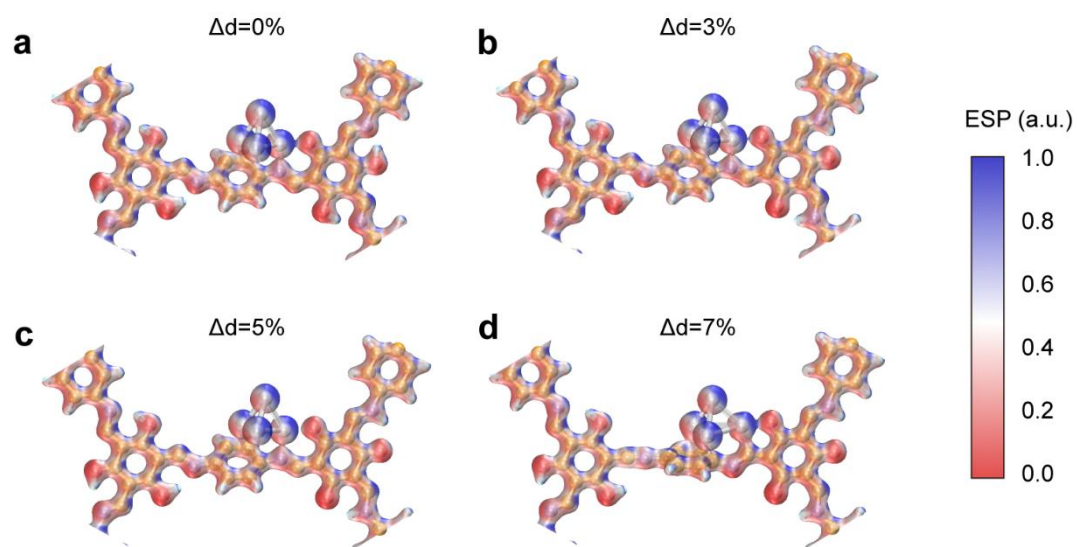


**Fig. S25** ESP calculations of different lattice strains: (a) TpPa-COF, (b) 3%, (c) 5%, (d) 7%.



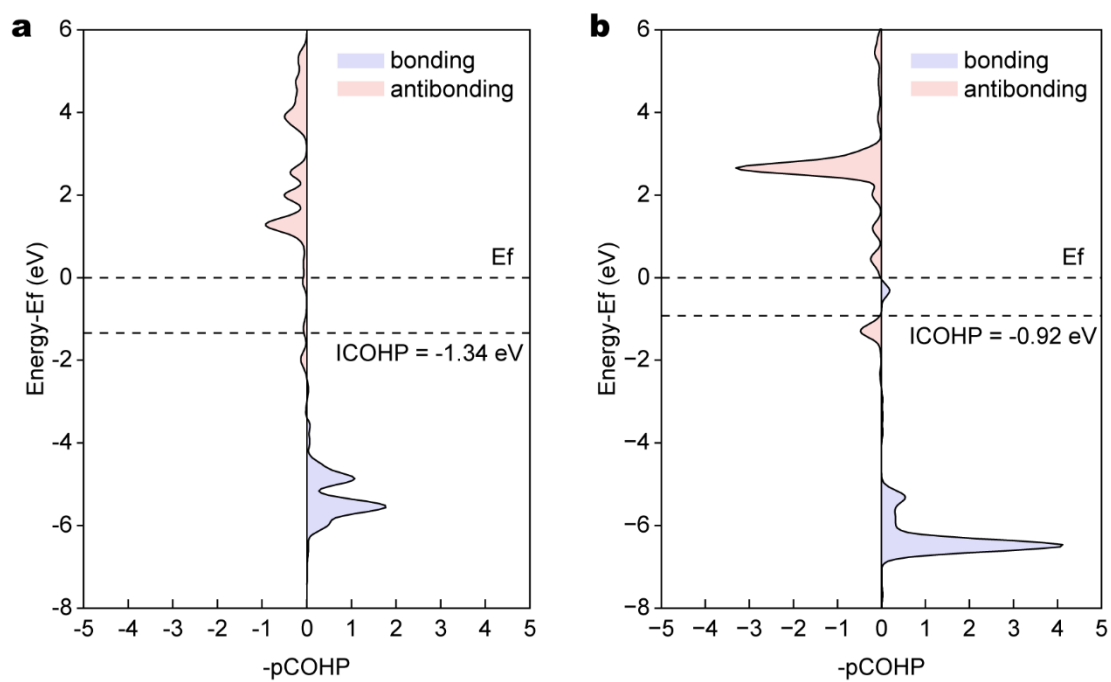


**Fig. S26** H-Pt Hamiltonian population analysis under (a) 5% and (b) 7% strains.

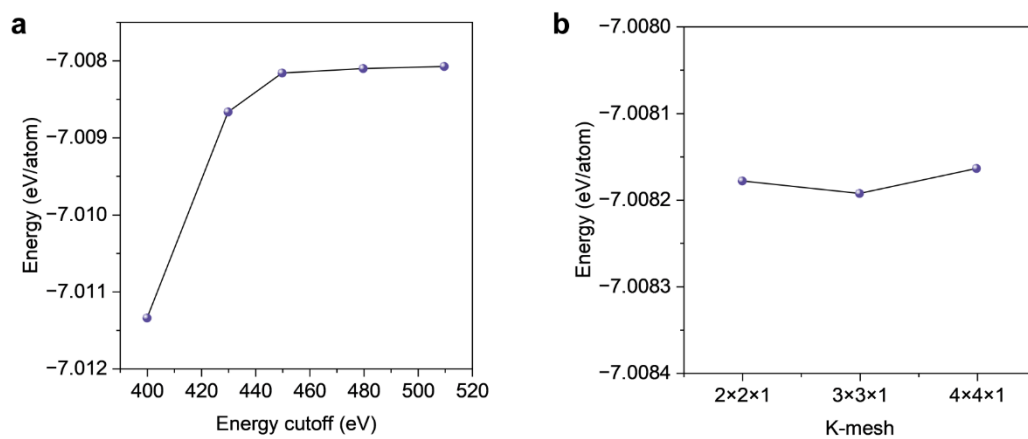


**Fig. S27** Convergence tests: (a) plane-wave energy cutoff; (b) k-point mesh.

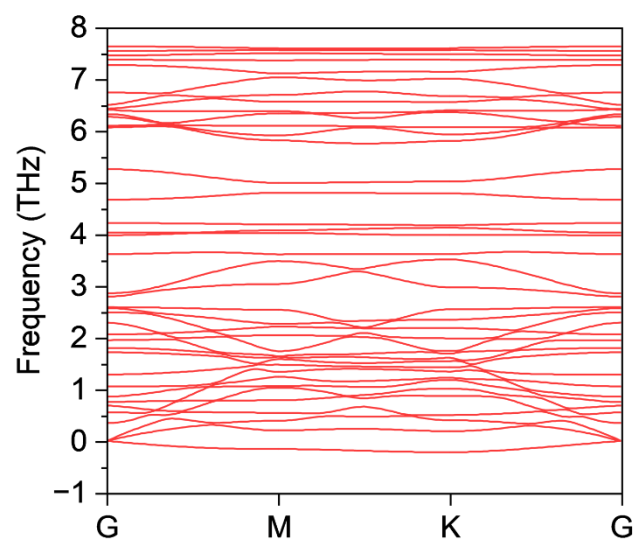


**Fig. S28** Harmonic phonon dispersion of TpPa-COF at 7% strain.

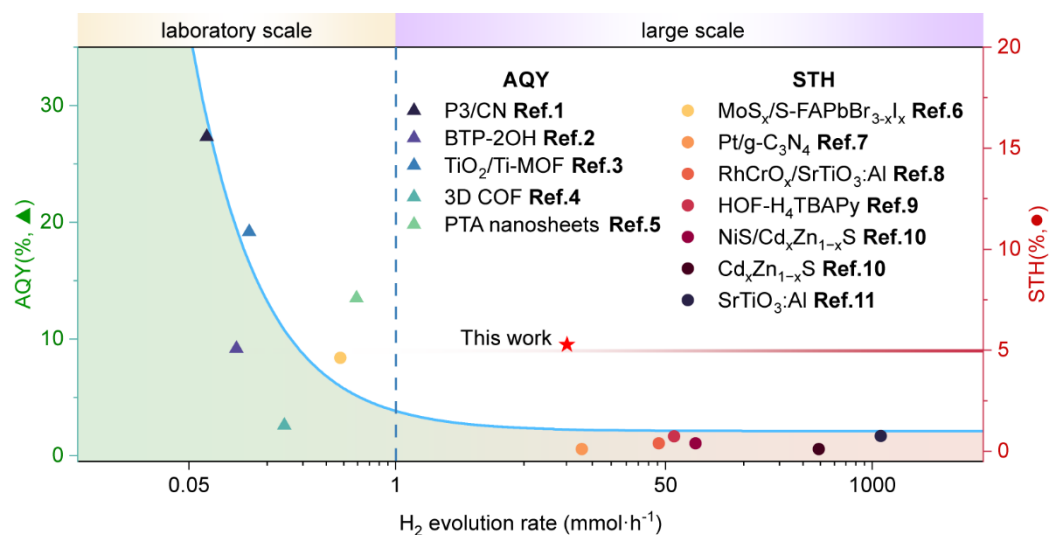


**Fig. S29** Comparison of hydrogen production efficiency from this experiment with previously reported high-efficiency hydrogen production works, where all obtained AQY values are measured under wavelengths at 420 nm, and all STH values are recorded under natural or simulated sunlight, the specific reference is showed in Table S3.

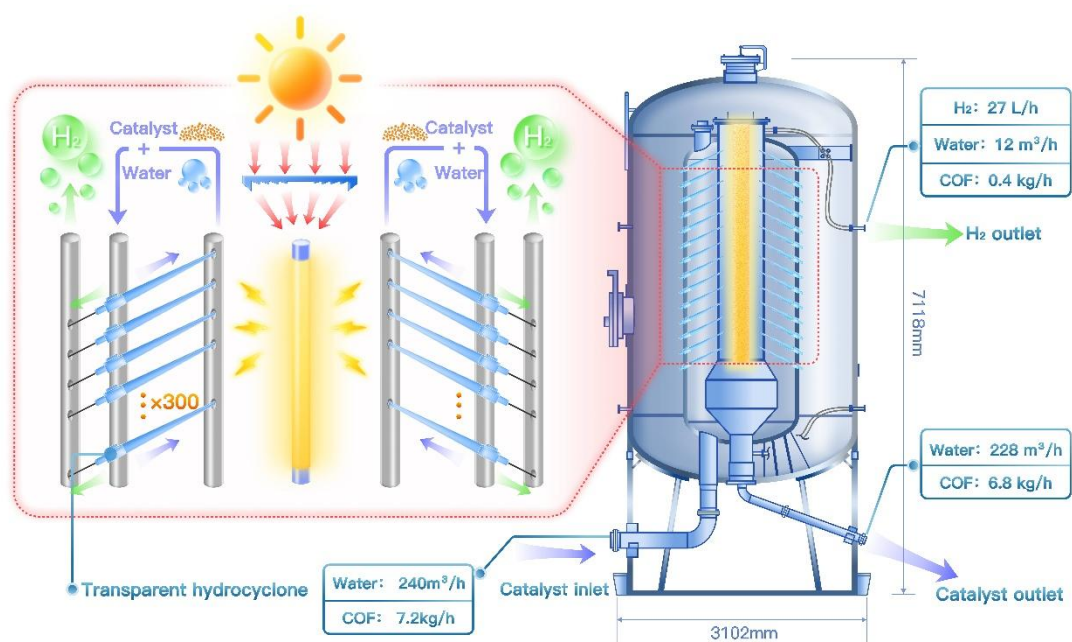


**Fig.S30** Scaled up for 100 times hydrocyclone-enhanced photocatalytic hydrogen production system.

## 4. Tables

**Table. S2** CFD-DEM parameters

	Particle	Wall
Poisson's ratio	0.25	0.25
Density (kg/m <sup>3</sup> )	3093	2500
Shear Modulus (Mpa)	1.00E+06	1.00E+06
Restitution coefficient	0.5	0.1
Static friction	0.5	0.2
Kinetic friction	0.01	0.01
Inlet velocity (m/s)	2.78	
Feeding Rate (kg/h)	9.84E-06	

**Table. S3** Photocatalytic hydrogen production efficiency across different scales

Catalysts	H <sub>2</sub> Evolution mmol/h	Catalyst dosage / mg (m <sup>2</sup> )	Light source	AQY	STH	Ref
Pt-COF	12.05	540	300W Xe 420 nm AM 1.5G (300 W m <sup>-2</sup> )	12.68	5.28	This work
P3/CN	0.065	50	300W Xe 520 nm	27.32		[1]
BTP-2OH	0.10	1	300W Xe 800 nm	9.17		[2]
TiO <sub>2</sub> /Ti-MOF	0.12	10	300W Xe 420 nm	19.17		[3]
3D COF	0.20	5	300W Xe 450 nm	2.58		[4]
MoS <sub>x</sub> /S-FAPbBr <sub>3-x</sub> I <sub>x</sub>	0.45	50	300W Xe > 420 nm		4.63	[5]
PTA nanosheets	0.57	7	300W Xe 420 nm	13.50		[6]
Pt@mp-CN	14.85	13300 (0.76m <sup>2</sup> )	natural sunlight		0.12	[7]
RhCrO <sub>x</sub> /SrTiO <sub>3</sub> :Al	45.36	1m <sup>2</sup>	natural sunlight simulated		0.40	[8]
HOF-H <sub>4</sub> TBAPy	56.66	0.50m <sup>2</sup>	sunlight (1,000 W m <sup>-2</sup> )		0.75	[9]
NiS/Cd <sub>x</sub> Zn <sub>1-x</sub> S	77.32	35000	natural sunlight		0.40	[10]
Cd <sub>x</sub> Zn <sub>1-x</sub> S	460.75	573390	natural sunlight		0.12	[10]
SrTiO <sub>3</sub> :Al	1130	100 m <sup>2</sup>	natural sunlight		0.76	[11]

**Table. S4** Gibbs free energy calibration data

Lattice strain	0% (eV)	3% (eV)	5% (eV)	7% (eV)	9% (eV)
$E_{H^*}$	-488.00	-485.92	-485.34	-486.59	-483.75
$E_{surface}$	-483.78	-481.977	-481.41	-482.67	-479.75
$\Delta E_{ZPE} +$ $\Delta U(0 \rightarrow T)$	0.21	0.21	0.20	0.20	0.21
$T\Delta S_H$	0.02	0.02	0.01	0.01	0.02
$\Delta G_{H^*}$	-0.61	-0.35	-0.33	-0.32	-0.40



## 5. Supplementary references

- [1] Yu F, Wang Z, Zhang S, et al. Molecular engineering of donor–acceptor conjugated polymer/g-C<sub>3</sub>N<sub>4</sub> heterostructures for significantly enhanced hydrogen evolution under visible-light irradiation. *Advanced Functional Materials*, 2018, 28(47): 1804512.
- [2] Liu X, Zhao Y, Ni Y, et al. Hydroxylated organic semiconductors for efficient photovoltaics and photocatalytic hydrogen evolution. *Energy & Environmental Science*, 2023, 16(9): 4065-4072.
- [3] He X, Ding Y, Huang Z, et al. Engineering a Self-Grown TiO<sub>2</sub>/Ti-MOF Heterojunction with Selectively Anchored High-Density Pt Single-Atomic Cocatalysts for Efficient Visible-Light-Driven Hydrogen Evolution. *Angewandte Chemie*, 2023, 135(25): e202217439.
- [4] Wang Y, Qiao Z, Li H, et al. Molecular Engineering for Modulating Photocatalytic Hydrogen Evolution of Fully Conjugated 3D Covalent Organic Frameworks. *Angewandte Chemie International Edition*, 2024: e202404726.
- [5] Xu T, Xie Y, Qi S, et al. Simultaneous Defect Passivation and Co-Catalyst Engineering Leads to Superior Photocatalytic Hydrogen Evolution on Metal Halide Perovskites. *Angewandte Chemie International Edition*, 2024: e202409945.
- [6] Guo Y, Zhou Q, Nan J, et al. Perylenetetracarboxylic acid nanosheets with internal electric fields and anisotropic charge migration for photocatalytic hydrogen evolution. *Nature Communications*, 2022, 13(1): 2067.
- [7] Schröder M, Kailasam K, Borgmeyer J, et al. Hydrogen evolution reaction in a large - scale reactor using a carbon nitride photocatalyst under natural sunlight irradiation. *Energy Technology*, 2015, 3(10): 1014-1017.
- [8] Goto Y, Hisatomi T, Wang Q, et al. A particulate photocatalyst water-splitting panel for large-scale solar hydrogen generation. *Joule*, 2018, 2(3): 509-520.
- [9] Zhou Q, Guo Y, Zhu Y. Photocatalytic sacrificial H<sub>2</sub> evolution dominated by micropore-confined exciton transfer in hydrogen-bonded organic frameworks. *Nature Catalysis*, 2023, 6(7): 574-584.
- [10] Wei Q, Yang Y, Liu H, et al. Experimental study on direct solar photocatalytic water splitting for hydrogen production using surface uniform concentrators. *International Journal of Hydrogen Energy*, 2018, 43(30): 13745-13753.
- [11] Nishiyama H, Yamada T, Nakabayashi M, et al. Photocatalytic solar hydrogen production from water on a 100-m<sup>2</sup> scale. *Nature*, 2021, 598(7880): 304-307.